Temperature Profiles, the Size of the Heat-affected Zone and Dilution in Electroslag Welding

T. DEBROY*, J. SZEKELY and T. W. EAGAR

Department of Materials Science and Engineering, Massachusetts Institute of Technology, Cambridge, MA 02139 (U.S.A.)

(Received October 28, 1981; in revised form April 1, 1982)

SUMMARY

A mathematical model was developed to represent the three-dimensional temperature field in the slag, the metal pool and the baseplate regions in the electroslag welding process. The spatially distributed heat generation patterns used in the calculations were obtained from the solution of the electric field equations.

The output from the model were the temperature fields in the baseplate, the dilution, the size of the heat-affected zone and the grain growth in the heat-affected zone. Reasonably good agreement was obtained between the predictions based on the model and experimental measurements reported in the literature and those obtained in the Welding Laboratory, Massachusetts Institute of Technology.

The two important findings that result from this work are that for electroslag welding systems the heat-affected zone is relatively uniform and its size is not markedly affected by the process parameters; furthermore, the percentage dilution is appreciably influenced by process parameters, such as the plate gap and the liquidus temperature.

1. INTRODUCTION

The electroslag welding (ESW) process is a potentially attractive operation for the welding of thick plates needed in the construction of ships, storage tanks, pressure vessels, bridges, buildings and other structures [1 - 4].

The major problem associated with ESW is that it tends to produce a large heat-affected zone, which may require renormalization (heat treatment) in order to obtain the necessary fracture toughness.

The previous work done in the modelling of the ESW process has pursued two specific directions. Work has been done to examine the nature of the fluid flow fields induced in the molten slag and in the metal pool by electromagnetic and buoyancy forces in idealized two-dimensional systems [5]. This modelling effort has shown that the nature of the flow field and the relative importance of the electromagnetic and the buoyancy forces are markedly affected by the geometry of the system.

In subsequent work [6] the temperature fields and the heat generation patterns in three-dimensional systems were examined. This research has shown that a reduction in the total heat input may be obtained by narrowing the plate gap and by using closely spaced multiple electrodes. It was also found that electrode asymmetry could lead to strongly maldistributed heat generation patterns.

This previous paper contributed an important intermediate step but was not able to address some crucial parts of the ESW problem, namely the effect of dilution, the explicit definition of the heat-affected zone and the effects of grain coarsening in this region. The purpose of the present work is to represent the heat generation pattern and the temperature profiles in the molten slag and in the metal pool, together with the transient temperature distribution in the baseplates. These two heat transfer processes are of course coupled and are made somewhat more complex by the dilution effect.

---

*Present address: Metallurgy Section, Department of Materials Science and Engineering, Pennsylvania State University, PA, U.S.A.

This more realistic representation will allow the explicit definition of the heat-affected zone, together with the grain-coarsening phenomena that take place in this region. Furthermore, an explicit relationship between the process parameters and the size of the heat-affected zone may be obtained, and it should be possible, for the first time, to obtain a direct comparison between the predictions based on the model and experimental measurements.

2. FORMULATION

A diagram of the ESW process is shown in Fig. 1. A consumable wire electrode is fed continuously into a molten slag pool, which is resistively heated by a current passing from the electrode through the molten slag and the metal pool to the baseplates. The heat generation and the convective motion within the molten slag cause the electrode to melt, and molten metal droplets descend through the slag into the metal pool, displacing the slag pool in an upward direction. Part of the thermal energy generated is transferred into the baseplate and, as a result, partial melting
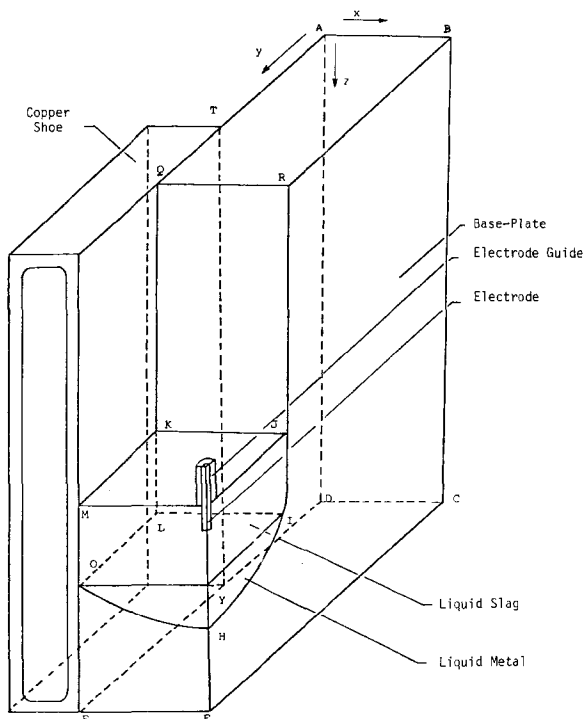
of the baseplate takes place. Two water-cooled copper "shoes" provide surfaces through which part of the thermal energy generated is being removed from the system. Subsequent to the melting process the solidification of the molten metal pool takes place, which causes the joining of the baseplates.

The mathematical representation of this process has to take into account the following physical phenomena.

(1) The passage of the current from the electrode through the slag and the metal pools to the baseplate is responsible for a spatially distributed heat generation pattern.

(2) The thermal energy is transferred in molten regions by conduction and by convection, the latter resulting from both buoyancy and electromagnetic forces.

(3) Heat transfer in the molten regions is also affected by the movement of the molten droplets and by the addition of the cold slag.

(4) Thermal energy is transferred in the baseplate by transient conduction and the time-dependent position of the boundary separating the molten and the solid metal regions is determined by a dynamic heat balance.

(5) Finally, knowledge of the temperature–time history within the solid baseplate enables the modelling of grain-coarsening phenomena which is a desired output of the calculations.

It follows that the representation of the problem requires (a) a statement of the appropriate electric field equations, together with Ohm's law in three dimensions, in order to obtain the spatially distributed heat generation pattern, (b) a statement of the three-dimensional heat conduction equations with due allowance for heat generation in the slag as well as heat transfer to the metal pool and the baseplate, incorporating the transient melting and solidification phenomena, and (c) a statement of the relationship for grain growth, incorporating the temperature–time history of the baseplate.

2.1. The heat generation pattern

In the calculations of the heat generation pattern we shall assume that all the voltage drop occurs across the slag layer, which is reasonable, because the electrical resistance of the slag phase is several thousand times that of the metal phase [7].

Fig. 1. Sketch of the ESW process.

The local heat generation rate Q_g may then be obtained from [6]

$$Q_g = J \cdot E \tag{1}$$

where J is the current density and E is the electric field.

2.2. Temperature profiles

The temperature profiles in the molten metal and slag phases are represented by the following relationships:

$$\nabla k_{eff} \nabla T + Q_s = 0 \tag{2a}$$

while the temperature profile in the baseplate is given by

$$\nabla k \nabla T = \rho C_p \frac{\partial T}{\partial t} \tag{2b}$$

The quantity k_{eff} appearing in eqn. (2) is a spatially dependent effective thermal conductivity, which incorporates the effects of the thermally and the electromagnetically driven flows [5, 6]. The values of k_{eff} used in the computation are given in Table 1.

The quantity Q_s is the spatially variable heat source and heat sink term, which has been defined in ref. 6.

2.3. Electrode melting

The rate at which the electrode melts was calculated using a heat balance of the following form:

$$Q_{el} = Q_t - Q_d - Q_{sl\,r} - Q_{sl-pl} - Q_{sl-Cu} - \\ - Q_{sl-m} - Q_r - Q_{el\,ch} \tag{3}$$

where Q_{el} (kW) is the heat transfer rate from the slag to the electrode and Q_{sl-pl}, Q_{sl-Cu} and Q_{sl-m} are the rates of heat transfer from the liquid slag to the baseplate, from the liquid slag to the copper shoe and from the liquid slag to the liquid metal pool respectively. These quantities are calculated from the temperature field by integrating the local

TABLE 1

Values of various parameters used for the calculation of temperature fields

Plate thickness	2.54×10^{-2} m; 5.08×10^{-2} m
Initial plate gap	1.9×10^{-2} m; 3.0×10^{-2} m; 10^{-2} m
Width of Cu shoe	1.02×10^{-1} m
Electrode radius r_{el}	1.2×10^{-3} m
Metal drop radius r_d	1.2×10^{-3} m
Depth of the slag pool	3.0×10^{-2} m
Electrode immersion in the slag	1.5×10^{-2} m for plates 2.54×10^{-2} m thick; 0.95×10^{-2} m for plates 5.08×10^{-2} m thick
Length of the baseplate	0.30 m; 0.61 m
Electrode voltage	37 V for plates 2.54×10^{-2} m thick; 45 V for plates 5.08×10^{-2} m thick
Current	Calculated in the program, approximately 500 A
Molten slag electrical conductivity σ	$375\ \Omega^{-1}\ m^{-1}$
Molten slag thermal conductivity k_{sl}	10.5×10^{-3} kJ ms^{-1} K^{-1}
Molten metal thermal conductivity k_m	2.1×10^{-2} kJ ms^{-1} K^{-1}
Heat transfer coefficient h_{ov} at the slag–cooling shoe interface	1.67 kJ m^{-2} s^{-1} K^{-1}
Heat transfer coefficient at the base plate–cooling shoe interface	0.13 kJ ms^{-1} K^{-1}
Convective heat transfer coefficient h_c at the baseplate surfaces	0.084 kJ ms^{-1} K^{-1}
Specific heat of the electrode	0.84 kJ kg^{-1}
Specific heat $C_{p\,m}$ of the liquid metal drops	0.84 kJ kg^{-1}
Specific heat $C_{p\,sl}$ of the slag	1.05 kJ kg^{-1}
Latent heat ΔH_{el} of fusion of the electrode	272 kJ kg^{-1}
Emissivity ϵ_{sl} of the free slag surface	0.6
Viscosity of the slag	1.0×10^{-2} kg ms^{-1}
Density ρ_m of the liquid metal	7×10^3 kg m^{-3}
Density ρ_{sl} of liquid slag	2.7×10^3 kg m^{-3}
Effective conductivity $k_{eff\,sl}$ of the slag phase	0.25 kJ ms^{-1} K^{-1} (in the bulk); 3.1×10^{-2} kJ ms^{-1} K^{-1} (near the walls)
Effective conductivity $k_{eff\,m}$ of the metal phase	0.13 kJ ms^{-1} K^{-1} (in the bulk); 6.5×10^{-2} kJ ms^{-1} K^{-1} (near the walls)

values of the heat flux at the respective surfaces.

Of the quantities appearing on the right-hand side of eqn. (11), Q_t is evaluated after the calculation of voltage distribution in the slag phase. The other quantities appearing on the right-hand side of eqn. (3) were evaluated iteratively together with the computation of the temperature field. The actual melting rate of the electrode is calculated from the following relationship:

$$Q_{el} = m\{C_{p\,m}(T_{l\,m} - T_a) + \Delta H_m\} \tag{4}$$

2.4. Temperature profile in the baseplate

The temperature profile in the baseplate was obtained by solving the previously given equation, eqn. (3); both the thermal conductivity and the specific heat were allowed to be temperature dependent.

In the present computation, low carbon steel was used and the following relationships were employed to describe the temperature dependence of the thermal conductivity [8] and the specific heat [9]:

$$k = 9.2 \times 10^{-2} - 5.86 \times 10^{-5} T \quad \text{for } T < 1050\,\text{K}$$
$$= 3.05 \times 10^{-2} \quad\quad\quad \text{for } T > 1050\,\text{K} \tag{5}$$

where k is expressed in kilowatts per milli-kelvin.

$$C_p = 0.46 + 4.18 \times 10^{-4} T \quad \text{for } T < 1000\,\text{K}$$
$$= 0.88 \quad\quad\quad\quad \text{for } T > 1000\,\text{K} \tag{6}$$

where C_p is expressed in kilojoules per kilogram kelvin.

2.5. Heat-affected zone, grain growth phenomena and dilution

Once the temperature profile is known in the baseplate, the size of the heat-affected zone may be evaluated. It is noted that the "heat-affected zone" is not a well-defined term but is generally used to designate the region in the base metal which has undergone significant structural changes due to the welding process. Quite often this structural change is directly attributable to grain growth.

It is generally assumed in the literature on welding [10] that the size of the heat-affected zone may be defined in terms of the locus of a peak temperature in the baseplate, which in turn affects the grain growth kinetics.

In the present case we shall make use of the fact that, for a wide variety of steels which have ferrite—pearlite, martensite and tempered martensite structures, the grain size can be calculated by assuming that the austenite grain size is zero at the finishing temperature of the austenite transformation. The following kinetic expression [11] is used to calculate the grain growth:

$$\frac{dD}{dt} = \frac{k'}{4D^3} e^{-A/RT} \tag{7}$$

where D (m) is the average grain diameter, k' (= 49.5 m s^{-1}) and A (= 531 kJ (g atom)$^{-1}$) are constants, characteristic of the kinetics of grain growth. R and T are the universal gas constant and the absolute temperature respectively.

It will be shown subsequently, through the solution of eqn. (7), that most of the grain growth occurs during the heating period, so that the locus of the temperature peaks is indeed a good measure of the size of the heat-affected zone.

Dilution, which is an important parameter, may be calculated at any time after the computation of the temperature profile. The base metal dilution can be calculated from the following equation:

$$m_b = \frac{Q_{sl-pl} - H_{sl-pl}}{\Delta H_m} \tag{8}$$

where Q_{sl-pl} (kW) and $(Q_{sl-pl} - H_{sl-pl})$ (kW) are the rate of heat transfer from the liquid slag to the baseplate and the rate of heat transfer from the molten region of the base-plate to the interior of the baseplate, while ΔH_m (kJ kg^{-1}) is the latent heat of fusion. These quantities are calculated from the temperature field by integrating the local values of the heat fluxes. The amount of base metal dilution is readily obtained from the following expression:

$$\text{dilution (\%)} = \frac{m_b}{m_b + m} \tag{9}$$

where m is the melting rate of the electrode.

3. COMPUTATIONAL PROCEDURE

A computational procedure is required to solve the electric field equations, eqns. (2) and (3), the steady state or quasi-steady state
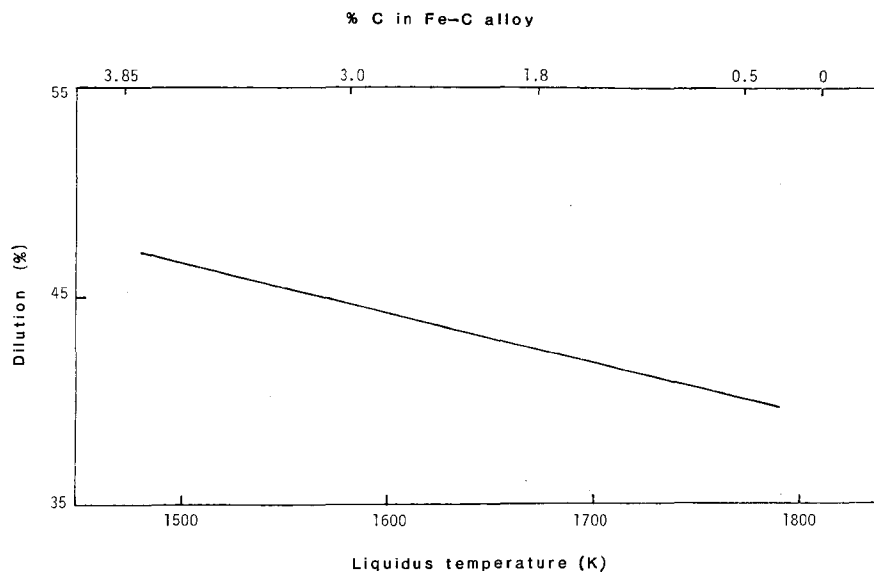
% C in Fe—C alloy

Fig. 2. Dilution *vs.* liquidus temperature of the baseplate material (plate dimensions, 0.47 m long, 0.61 m wide and 0.025 m thick; welding voltage, 37 V; plate gap, 0.03 m; electrode immersion, 0.015 m).

heat conduction equations in the molten regions and the transient heat flow equation in the baseplate. The electric field equations are uncoupled from the heat flow equations and thus may be solved independently. However, the heat flow equations in the molten region and in the baseplate are coupled through boundary conditions and have to be solved together by the use of an iterative procedure.

The electric field equations were solved first using a finite difference form and non-uniformly spaced rectangular grids. The solution of the electric field equations provided the information necessary to calculate heat generation patterns.

A flexible grid system was employed for the baseplate, which was redefined at each time step, so as to allow a large number of grid points in the vicinity of the liquid slag– baseplate and liquid metal–baseplate inter-faces where the temperature gradients were the steepest.*

The next step was to estimate the dilution, *i.e.* the position of the melt line, and then to solve the heat flow equations, for the known heat generation pattern. At this stage the temperature boundary condition imposed on the molten system was that the boundary

---

*A detailed discussion of the computational procedure is available in ref. 12.

with the solid surface had to be at the melting temperature. The actual melting temperature depended on the material properties as illustrated in Fig. 2.

The subsequent step involved the solution of the transient conduction equation for the baseplate, and then the dilution was calculated. This calculated dilution was compared with that assumed in the computation of the temperature field in the molten region and, if necessary, the calculation was repeated until satisfactory agreement was reached.

Usually the number of grids used was about 4300, and a typical calculation took about 500 s of central processing time on the IBM 370 digital computer at the Massachusetts Institute of Technology.

4. COMPUTED RESULTS

In the following we shall present a selection of the computed results which include the spatially distributed heat generation patterns, the temperature fields in the molten regions and in the baseplate, the dilution and grain growth within the heat-affected zone.

In a previous paper, extensive information has been presented on the molten regions; for this reason, in the present work, emphasis will be placed on describing the behavior of the baseplate. The principal parameters used
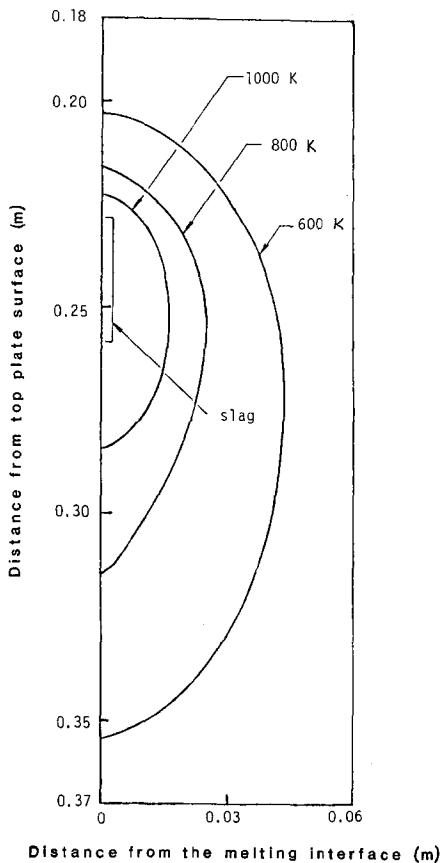
Fig. 3. Temperature map at the half-thickness and at the midsection ($t^* = 0.5$; plate dimensions, 0.47 m long, 0.61 m wide and 0.025 m thick; welding voltage, 37 V; electrode immersion, 1.5×10^{-2} m).

in the computation are summarized in Table 1. These are thought to be typical of the values encountered in the welding of mild steel plates.

4.1. Temperature distribution

Figure 3 shows the computed temperature distribution, for a baseplate 2.54×10^{-2} m thick, 0.47 m long and 0.61 m wide, at a time that corresponds to half of the total time required for the completion of the weld.

The isotherms exhibit the typical behavior expected for a moving distributed heat source, and the location of the temperature maximum corresponds appropriately to the level of the slag−metal pool. While the isotherms depicted in Fig. 3 are qualitatively similar to curves that could be generated using a moving distributed heat source, in the present case this heat source was evaluated in a fairly rigorous manner by solving the appropriate electric field and heat flow equations rather than by treating the heat source as a fictitious quantity.

Figure 4 is a plot of the fraction of heat loss from the baseplate as a function of the dimensionless time. A more detailed breakdown of the heat balance is given in Table 2. Inspection of Fig. 4 shows that the distribution of the fractional heat loss varies quite appreciably during the course of the weld. During the initial stages most of the thermal
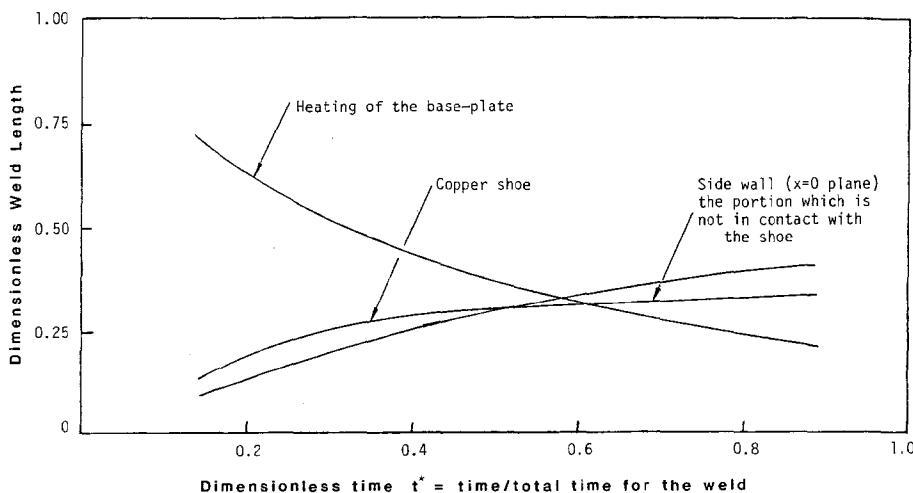

Fig. 4. Predominant sources of heat loss from the baseplate (plate dimensions, 0.47 m long, 0.51 m wide and 0.025 m thick; welding voltage, 37 V; plate gap, 0.03 m; electrode immersion, 0.015 m; weld speed $u_w = 3.1 \times 10^{-4}$ m s^{-1}).

TABLE 2

Heat balance in the baseplate based on one-half of
one of the baseplates (dimensionless time $t^* = 0.5$)

| Cause	Heat $(J\,s^{-1})$	Heat (%)
Gain		
Conduction from the slag to the melting surface	1000	
Less heat necessary for the melting of the baseplate	94.6	
Heat conducted from the slag—baseplate interface to the baseplate	905.4	52.8
Conduction from the solidifying interface in contact with the liquid metal to the baseplate	809.2	47.2
Total	1714.6	100
Loss		
Heating of the baseplate (unsteady state term)	624.3	36.2
Conduction loss through the following surfaces		
Side surface ($x = 0$ plane)	1048	60.9
End of the baseplate ($y = 0$ plane)	0.0	0.0
Loss through the vertical surface prepared for welding	20.5	1.2
Bottom plane	28.5	1.7
Top plane	0.8	0.0
Total	1722.1	100.0
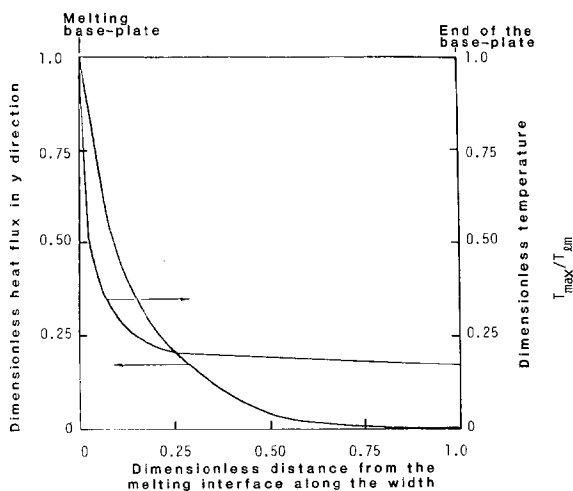
Fig. 5. Heat flux and temperature *vs.* distance along
the width of the baseplate ($t^* = 0.5$; plate dimensions,
0.47 m long, 0.61 m wide and 0.025 m thick; welding
voltage, 37 V; plate gap, 0.03 m; electrode immersion,
0.015 m; weld speed $u_w = 3.1 \times 10^{-4}$ m s^{-1}).

energy is being used to heat up the base-
plate, while during the latter stages the
thermal energy is more uniform distrib-
uted.

The data shown in Fig. 4 emphasize the
transient nature of this process which has two
important implications. One of these is that
the properties of the weld may exhibit
significant spatial variations; the other is that
great care has to be taken in the selection of
the test piece geometry, in order to reproduce
faithfully the conditions in production scale
operations.

Figure 5 is a plot of the dimensionless heat
flux into the baseplate and the dimensionless
temperature at the central plane at $t = 0.5$.
This central plane temperature is of course
the maximum at any given vertical position,
provided that symmetry is observed [6]. It
can be seen that both the temperature and
the heat flux into the baseplate decrease quite
sharply with the distance from the weld.

The model developed in the paper enables
a direct comparison to be drawn between the
theoretical predictions and experimental
measurements reported in the literature. This
is done in Fig. 6 using the data reported by
Benter *et al.* [2]. Since the model did not
incorporate the effect of the starting tab,
a 1 min "starting delay" was made to
represent this phenomenon. Inspection of
Fig. 6 shows very good agreement between
the predictions and the measurements.

Since the size of the heat-affected zone
plays an important role in determining the
mechanical properties of welds, it is of
interest to examine the implication of the
computed results regarding the size of the
heat-affected zone.

Figure 7 is a map of the peak temperatures,
in terms of the isotherms. The full line
represents the "standard conditions" while
the broken lines and the chain lines represent
results that have been computed for other
conditions.

As seen in Fig. 7, it is quite remarkable
that, notwithstanding the transient nature of
the process, the actual size of the heat-
affected zone as evidenced by the position of
the isotherms appears to be quite uniform.

Figure 8 shows the time dependence of
temperature at a particular location, together
with the variation in the grain size, as deter-
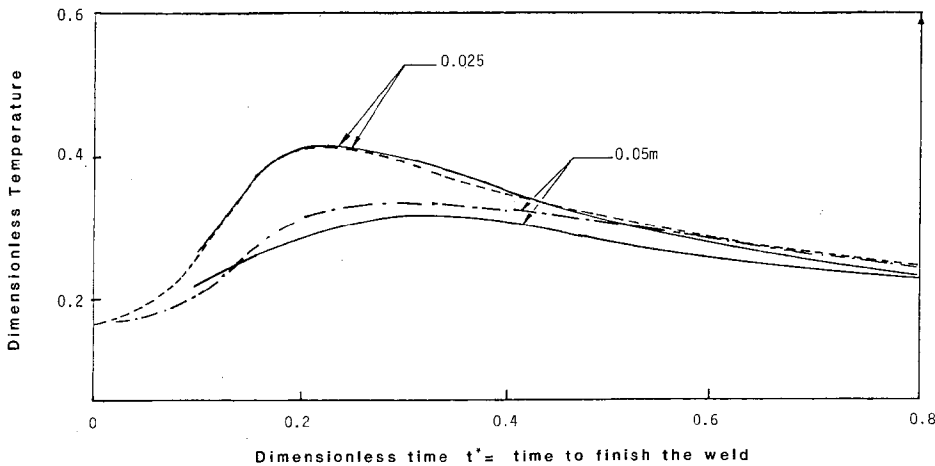mined by the integration of eqn. (7).

Fig. 6. Temperature at monitoring location *vs.* time, where the monitoring locations are at the half-thickness midsections at the bottom end of the baseplate at the distances indicated on the graphs (plate dimensions, 0.47 m long, 0.61 m wide and 0.02 m thick; welding voltage, 37 V; plate gap, 0.03 m; electrode immersion, 0.015 m; weld speed $u_w = 3.1 \times 10^{-4}$ m s^{-1}): — — —, experimental data of Benter *et al.* [2]; ———, model prediction.
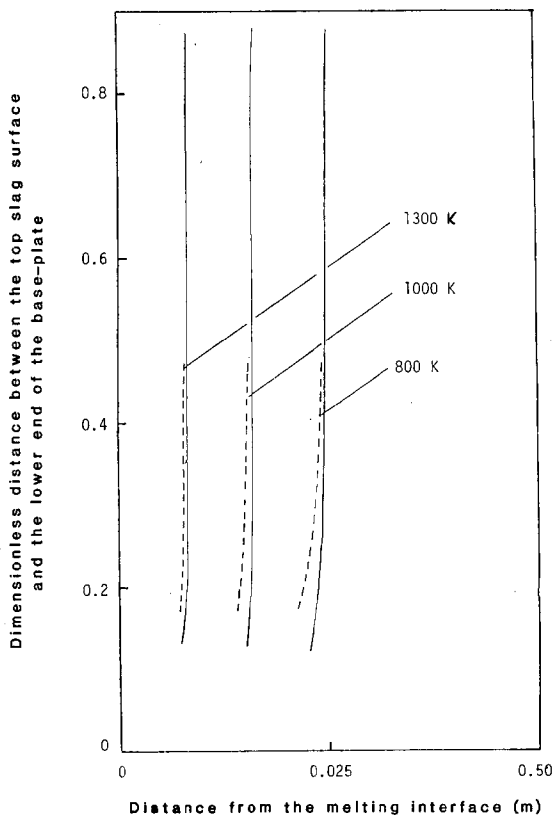

Fig. 7. Heat-affected zone size expressed as a function of peak temperatures: ———, the experimental conditions mentioned in Fig. 8 caption: — — —, for a weld with plate dimensions 0.3 m long, 0.3 m wide and 0.05 m thick, a welding voltage of 45 V, a plate gap of 1.9×10^{-2} m and an electrode immersion of 0.95×10^{-2}.

The temperature is seen to exhibit a characteristic peak, while the grain size tends to reach a plateau. Most of the grain growth occurs in the vicinity of the peak temperature, during the heating part of the cycle, which is fully consistent with the fact that grain growth is an activated process which is inhibited by the existence of large grains. It should be noted that the initial grain size has very little effect on the final grain size, unless the initial structure is very coarse. This behavior indicates that rapidly cooling the welded specimens after the completion of the weld, as suggested by some investigators, is unlikely to have any effect on the final structure obtained.

Figure 9 shows the effect of the plate gap on the size of the heat-affected zone, represented by plotting the area between the plane of fusion and the 1300 and 1000 K isotherms. It can be seen that the size of the heat-affected zone is not affected by the plate gap. Since the heat input has to be proportional to the plate gap, the important implication of Fig. 2 is that the size of the heat-affected zone does not appear to be significantly affected by the heat input. This finding appears to be contrary to previously held views.

Figure 10 is a plot of the percentage dilution, defined earlier in eqn. (9), against a dimensionless distance from the top of the weld. Although the dilution is initially low,
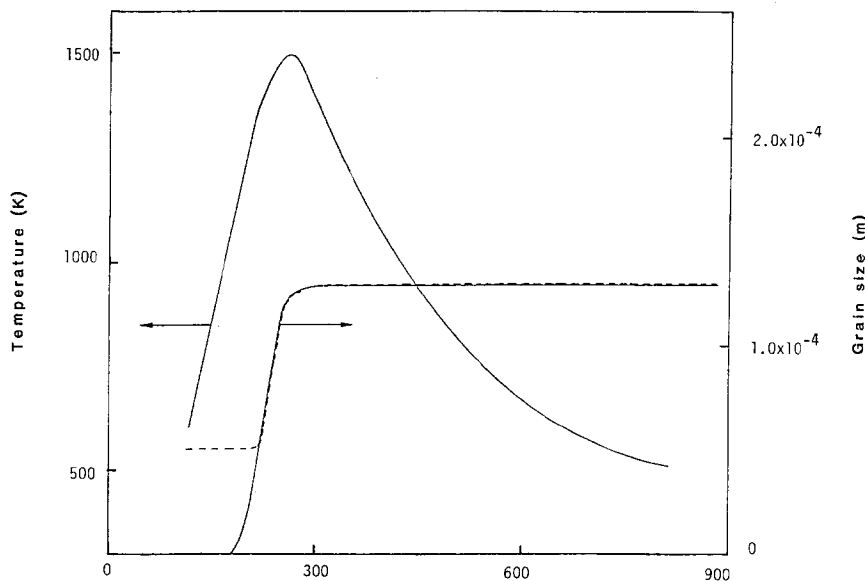
Fig. 8. Temperature and grain growth at a monitoring location 2.0×10^{-4} m from the melting interface, 5.0×10^{-2} m from the lower end of the baseplate at the half-thickness of the welding voltage (37 V) (plate gap, 0.03 m): — — —, initial grain size, 0.5×10^{-4} m; ———, initial grain size, 0 m.
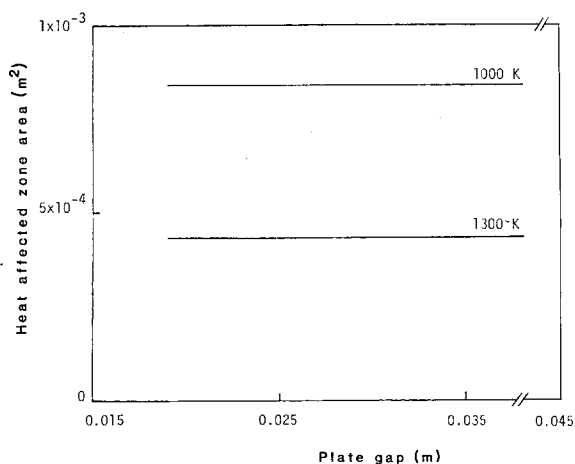

Fig. 9. Heat-affected zone area calculated from the locus of the peak temperatures as a function of plate gap for different peak temperatures (plate dimensions, 0.3 m long, 0.3 m wide and 0.04 m thick; welding voltage, 45 V; electrode immersion, 0.95×10^{-2} m).

it attains a more or less steady value maintained over most of the length of the weld and finally increases as the top of the plate is approached. This behavior seems to be reasonable because during the initial stages most of the thermal energy is being used to preheat the plate, while a quasi-steady-type heat balance is being maintained over most of the time period corresponding to the horizontal part of the curve. It should be

noted that the initially low level of dilution is usually compensated for by using a starting tab.

Figure 2 shows calculations depicting the effect of the liquidus temperature of the base-plate on the percentage dilution. It can be seen that, the lower the liquidus temperature, the higher is the percentage dilution. Although it is not usual to weld high carbon steels, the implications of Fig. 2 are quite interesting regarding the welding behavior of certain alloy steels, where there may be a significant variation in the liquidus temperature.

Finally, Fig. 11 shows the experimental measurements of Ricci [4] on the effect of the plate gap on the percentage dilution. The theoretical predictions based on the model are also shown for comparison. It can be seen that the experimental measurements do exhibit appreciable scatter. This scatter is attributable to the fact that the results were obtained as part of a statistically designed series, where a number of parameters (such as the voltage, the current, the flux composition and the slag pool depth), in addition to the plate gap shown as the abscissa, were varied. None the less, the data appear to be consistent with the theoretical predictions, indicating that an increased plate gap will reduce the dilution, a finding which may be readily supported by physical reasoning.
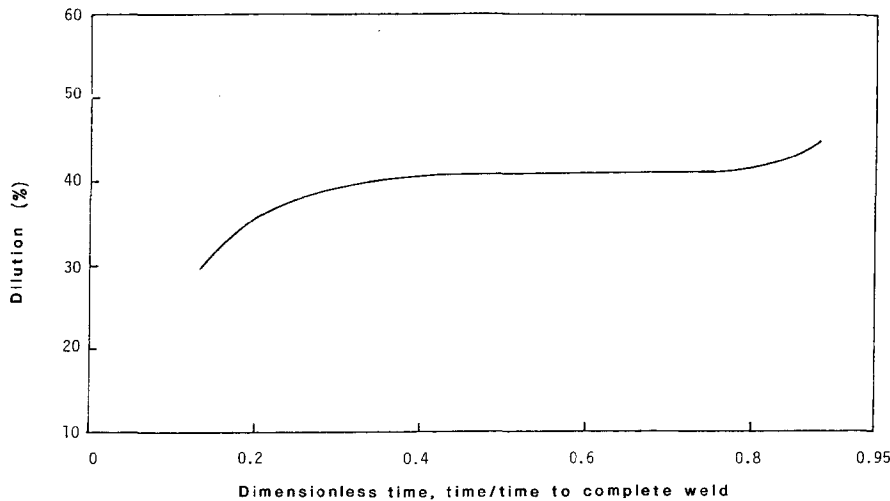
190

Fig. 10. Dilution *vs.* time (plate dimensions, 0.47 m long, 0.61 m wide and 0.025 m thick; welding voltage, 37 V; plate gap, 0.03 m; electrode immersion, 0.015 m; weld speed $u_w = 3.1 \times 10^{-4}$ m s^{-1}).
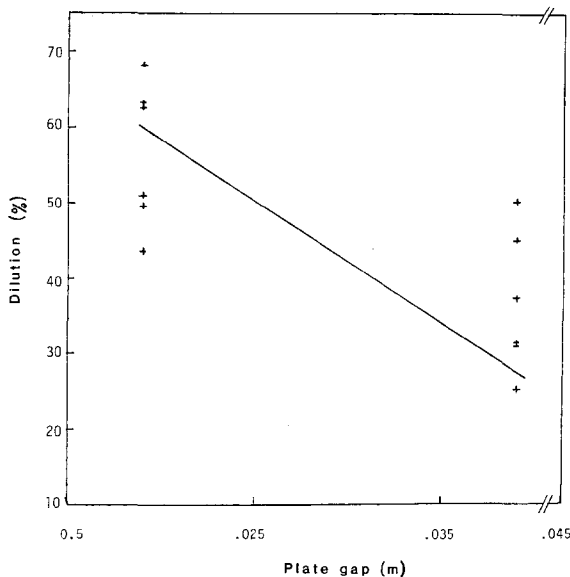

Fig. 11. Dilution *vs.* plate gap (plate dimensions, 0.3 m long, 0.3 m wide and 0.05 m thick; welding voltage, 45 V; electrode immersion, 0.095 m): +, experimental data of Ricci [4]; ———, model predictions.

5. DISCUSSION

In this paper a mathematical model has been presented to describe the three-dimensional temperature fields in the molten slag and metal regions and in the baseplates in the ESW process. The model enabled the calculation of the temperature fields in the baseplate, the dilution, the size of the heat-

affected zone and the grain growth in the heat-affected zone. A direct comparison was possible between predictions and experimental measurements; in general, good agreement was obtained.

It is considered that, in addition to providing a reasonable mathematical description of the ESW process, two important findings were made as a result of the mathematical modelling effort. One of these is that the heat-affected zone is relatively uniform and is not markedly affected by any of the process parameters. The other is that the percentage dilution is affected by process parameters, such as the plate gap and the liquidus temperature, to a significant extent. The apparent sensitivity of the percentage dilution to the overall heat balance is clearly illustrated in Table 2.

It is of interest to note that the percentage dilution *per se* has very little effect on the size of the heat-affected zone, a finding which appears to contradict earlier views [11].

The important conclusion to be drawn is that, by process modifications such as changing the plate gap, the power input or the welding speed is unlikely to produce dramatic changes in the size of the heat-affected zone.

At first sight the relative uniformity of the heat-affected zone may be surprising; furthermore it is not immediately obvious why the plate gap should not affect the thickness of the heat-affected zone, in view of the fact that the plate gap is known to have a marked influence on the total heat input. Figure 3 has

shown that the isotherms are essentially parallel at a position corresponding to that of the heat source which will thus account for the relatively uniform width of the heat-affected zone, notwithstanding the transient nature of the process. Furthermore, variations in the plate gap are compensated for by the travel speed; thus, for narrower gaps, faster welding speeds may be used. As the travel speed is increased, steeper gradients are established in the slag pool, resulting in higher heat fluxes to the baseplate. However, the melting of the baseplate acts as a buffer, which prevents additional thermal energy from being transferred into the baseplate.

The finding that the percentage dilution has little effect on the size of the heat-affected zone may be explained by the fact that the actual width of the heat-affected zone is measured from the fusion line rather than from the original plate surface. The boundary condition at this fusion line is the melting temperature of the plate and the gradients within the baseplate adjacent to this fusion line are largely controlled by the thermal conductivity of the solid steel.

ACKNOWLEDGMENT

NOMENCLATURE

A	constant, characteristic of the grain growth kinetics
C_p	specific heat of the baseplate (kJ kg^{-1} K^{-1})
$C_{p\,m}$	specific heat of the liquid metal (kJ kg^{-1} K^{-1})
$C_{p\,sl}$	specific heat of the slag (kJ kg^{-1} K^{-1})
D	average grain diameter (m)
E	electric field (V m^{-1})
h_c	heat transfer coefficient at the baseplate surface (kJ m^{-2} s^{-1} K^{-1})
h_{ov}	overall heat transfer coefficient at the slag−copper shoe interface (kJ m^{-2} s^{-1} K^{-1})

H_{sl-pl}	heat transferred at the slag−plate interface
J	current density (A m^{-2})
k	thermal conductivity (kJ ms^{-1} K^{-1})
k_{eff}	effective thermal conductivity (kJ ms^{-1} K^{-1})
$k_{eff\,m}$	effective thermal conductivity of the metal (kJ ms^{-1} K^{-1})
$k_{eff\,sl}$	effective thermal conductivity of the slag (kJ ms^{-1} K^{-1})
k_m	molten metal thermal conductivity (kJ ms^{-1} K^{-1})
k_{sl}	thermal conductivity of the slag
k'	constant, characteristic of the grain growth kinetics
m	electrode melting rate (kg s^{-1})
m_b	base metal dilution
Q_d	heat transfer rate from the molten slag to metal by liquid metal drops (kJ s^{-1})
Q_{el}	heat transfer rate from the slag to the electrode (kJ s^{-1})
$Q_{el\,ch}$	heat equivalent of the energy loss due to electrochemical effects (kJ s^{-1})
Q_g	local heat generation rate (kJ m^{-3} s^{-1})
Q_r	rate of heat loss by radiation from the surface of the liquid slag (kJ s^{-1})
Q_s	local heat loss rate (kJ m^{-3} s^{-1})
Q_{sl-Cu}	heat transfer rate from the slag to the copper shoe (kJ s^{-1})
Q_{sl-m}	heat transfer rate from the slag to the molten metal (kJ s^{-1})
Q_{sl-pl}	heat transfer rate from the slag to the baseplate (kJ s^{-1})
$Q_{sl\,r}$	heat required per unit time to heat the cold slag (kJ)
Q_t	total power dissipation rate (kJ s^{-1})
r_d	radius of the liquid metal droplet (m)
r_{el}	radius of the electrode wire (m)
R	universal gas constant
t	time
t_f	time required to finish the weld
t^*	dimensionless time; time divided by the finishing time
T	temperature in the computation domain; absolute temperature (K)
T_a	ambient temperature (K)
$T_{l\,m}$	melting point of the metal (K)
T_{max}	maximum temperature for a y = constant plane at a given time (K)
u_w	weld speed (m s^{-1})
x	x coordinate (m)

y	y coordinate (m)
z	z coordinate (m)
ΔH_{el}	latent heat of fusion of the electrode (kJ kg^{-1})
ΔH_m	latent heat of fusion of the metal (kJ kg^{-1})
ΔH_{sl}	latent heat of fusion of the slag (kJ kg^{-1})
ϵ_{sl}	emissivity of the free slag surface
ρ	density of baseplate (kg m^{-3})
ρ_m	density of the liquid metal (kg m^{-3})
ρ_{sl}	density of the slag (kg m^{-3})
σ	electrical conductivity of the slag ($\Omega^{-1}\,\text{m}^{-1}$)

REFERENCES

1 B. E. Paton, *Electroslag Welding*, American Welding Society, New York, 1962.
2 W. P. Benter, Jr., P. L. Konkol, B. M. Kapadia, A. K. Shoemaker and J. F. Sovak, Acceptance criteria for electroslag weldments in bridges, phase I, *Final Rep.*, April 1977, p. A-5 (U.S. Steel Corporation).
3 J. D. Harrison, *Metal Constr. Br. Weld. J.*, *1* (8) (1969) 366 - 370.
4 W. S. Ricci, The influence of process parameters on the size of the heat affected zone during electroslag welding, *M.S. Thesis*, Massachusetts Institute of Technology, 1979.
5 A. H. Dilawari, J. Szekely and T. W. Eagar, *Metall. Trans. B*, *9* (1978) 339.
6 T. Debroy, J. Szekely and T. W. Eagar, *Metall. Trans. B*, (1980) 593.
7 A. H. Dilawari and J. Szekely, *Metall. Trans. B*, *8* (1977) 227.
8 Y. S. Touloukin *et al.*, Thermal conductivity, in *Metallic Elements and Alloys, Thermophysical Properties of Matter*, Plenum, New York, 1970.
9 Y. S. Touloukin *et al.*, Specific heat, in *Metallic Elements and Alloys, Thermophysical Properties of Matter*, Plenum, New York, 1970.
10 *Welding Handbook*, Vol. 1, American Welding Society, Miami, FL, 1976.
11 H. Ikawa, S. Shin, H. Oshige and Y. Makuchi, *Trans. Jpn. Weld. Soc.*, *8* (2) (1977) 126.
12 T. Debroy, J. Szekely and T. W. Eagar, in *Modelling of Casting and Welding Processes*, Metallurgical Society of AIME, New York, 1981, p. 197.

APPENDIX A

A.1. Boundary conditions for the calculation of temperature profiles for the liquid slag and liquid metal

A.1.1. Top slag surface

$$k_{\text{eff sl}}\frac{\partial T}{\partial z} = \frac{1}{2}\epsilon\sigma_S T^4 \tag{A1}$$

A.1.2. Plate surface–slag interface

$$T = T_{l\,m} \text{ at } y = y_i \text{ and } y = y_f \tag{A2}$$

for all values of x and z.

A.1.3. Cooling shoe–slag interface

$$k_{sl}\frac{\partial T}{\partial x} = h_{ov}(T - T_a) \tag{A3}$$

A.1.4. Slag–liquid metal interface

$$k_{\text{eff sl}}\left(\frac{\partial T}{\partial z}\right)_{sl} = k_{\text{eff m}}\left(\frac{\partial T}{\partial z}\right)_m \tag{A4}$$

A.1.5. Liquid metal–plate interface

In the present computations the liquid metal pool shape was prescribed to be approximately hemispherical. At the solid–liquid metal interface,

$$T = T_{l\,m} \tag{A5}$$

A.1.6. For the baseplate

The following boundary conditions are used for the computation of temperature profile in the baseplate. Figure 1 shows the different planes mentioned in this section.

(i) At the vertical surface of the plate (ABCD plane),

$$k_{pl}\frac{\partial T}{\partial y} = h_c(T - T_a) \tag{A6}$$

(ii) At the bottom end of the plate (CDEF plane),

$$-k_{pl}\frac{\partial T}{\partial z} = h_c(T - T_a) \tag{A7}$$

(iii) In the midsection symmetry plane (RJIHFCB plane),

$$\frac{\partial T}{\partial x} = 0 \tag{A8}$$

(iv) At the plate–cooling shoe interface (TYEOLQ plane),

$$k_{pl}\frac{\partial T}{\partial x} = h_c(T - T_a) \tag{A9}$$

(v) At the vertical surface of the plate (ADYT plane),

$$k_{pl}\frac{\partial T}{\partial x} = h_c(T - T_a) \tag{A10}$$

(vi) At the top surface of the plate (ABRQ plane),

$$k_{pl} \frac{\partial T}{\partial z} = h_c(T - T_a) \qquad (A11)$$

(vii) In the midsection symmetry plane (EFHO plane),

$$\frac{\partial T}{\partial y} = 0 \qquad (A12)$$

(viii) At the curved surface at the liquid metal–plate surface (OLIH plane),

$$T = T_{l\,m} \qquad (A13)$$

(ix) At the liquid slag–plate interface (KJIL plane),

$$T = T_{l\,m} \qquad (A14)$$

(x) At the vertical surface of the plate (QRJL plane),

$$k_{pl} \frac{\partial T}{\partial y} = \sigma F_{s \to \boxtimes}(\epsilon_{sl} T_{sl\,av}^{4} - \epsilon T^{4}) - h_c(T - T_a)$$
$$\qquad (A15)$$

Nomenclature for Appendix A

$F_{s \to \boxtimes}$ view factor

h_c heat transfer coefficient at the base-

plate surface (kJ m^{-2} s^{-1} K^{-1})

h_{ov} overall heat transfer coefficient at the slag–copper shoe interface (kJ m^{-2} s^{-1} K^{-1})

$k_{eff\,m}$ effective thermal conductivity of the metal (kJ ms^{-1} K^{-1})

$k_{eff\,sl}$ effective thermal conductivity of the slag (kJ ms^{-1} K^{-1})

k_{pl} thermal conductivity of the baseplate (kJ ms^{-1} K^{-1})

k_{sl} thermal conductivity of the slag (kJ ms^{-1} K^{-1})

T temperature in the computation domain; absolute temperature (K)

T_a ambient temperature (K)

$T_{l\,m}$ melting point of the metal (K)

$T_{sl\,av}$ average temperature of the top slag surface (K)

x x coordinate (m)

y y coordinate (m)

y_f y coordinate of the end of the computation domain (m)

y_i y coordinate of the start of the computation domain (m)

z z coordinate

ϵ emissivity of the baseplate

ϵ_{sl} emissivity of the free slag surface

σ_S the Stefan–Boltzmann constant